

Surface Material Characterization from Multi-band Optical Observations

Doyle Hall

AMOS - Boeing LTS, Kihei, HI and Colorado Springs, CO

1 SUMMARY

Ground-based optical and radar sites routinely acquire resolved images of satellites. These resolved images provide the means to construct accurate wire-frame models of the observed body, as well as an understanding of its orientation as a function of time. Unfortunately, because such images are typically acquired in a single spectral band, they provide little information on the types of materials covering the satellite's various surfaces. Detailed surface material characterization generally requires spectrometric and/or multi-band photometric measurements. Fortunately, many instruments provide such multi-band information (e.g., spectrographs and multi-channel photometers). However, these sensors often measure the brightness of the entire satellite, with no spatial resolution at all. Because such whole-body measurements represent a summation of contributions from many reflecting surfaces, an "un-mixing" or inversion process must be employed to determine the materials covering each of the satellite's individual sub-components. The first section of this paper describes the inversion theory required to retrieve satellite surface material properties from temporal sequences of whole-body multi-band brightness measurements. The inversion requires the following as input: 1) a set of multi-band measurements of a satellite's reflected-sunlight brightness, 2) the satellite's wire-frame model, including each major component capable of reflecting sunlight, 3) the satellite's attitude, specifying the body's orientation at the time of each multi-band measurement, and 4) a database of bi-directional reflection distribution functions for a set of candidate surface materials. As output, the inversion process yields estimates of the fraction of each major satellite component covered by each candidate material. The second section of the paper describes several tests of the method by applying it to simulated multi-band observations of a cubical satellite with different materials on each of its six faces. The tests indicate that the inversion method successfully retrieves the six known materials when provided a complete noise-free scan of the cube as input. The method also performs reasonably well when confronted with the adverse effects of measurement noise, superfluous or unknown candidate materials, and incomplete observations.

This research funded by the Air Force Office of Scientific Research.

2 INTRODUCTION

Ground-based optical and radar sites routinely acquire resolved images of satellites, yielding a great deal of knowledge about orbiting spacecraft. In particular, the Air Force Maui Optical and Supercomputing (AMOS) Detachment on Maui has been acquiring optical imagery using two work-horse imagery systems. The AMOS Advanced Electro-optical System (AEOS) 3.6m telescope provides visible-band and long-wavelength thermal infrared images with adaptive optics compensation to remove atmospheric blurring. In addition, the AMOS Gemini 1.6m telescope system provides daytime visible-band and near-infrared speckle images. These systems reveal a great deal of resolvable detail for satellites in low-Earth orbit (LEO), especially after the data undergo post-processing enhancement at the AFRL Maui High Performance Computing Center. Other observatories, such as Starfire Optical Range (SOR), as well as some ground-based radar sites, also acquire images of comparable quality. Using such images, detailed wire-frame models of the observed satellites can be assembled and aligned to the images using existing software tools. This process essentially translates the two-dimensional imagery into detailed three-dimensional information about the sizes, shapes, and relative orientations of various spacecraft surfaces. Unfortunately, such image analysis procedures provide little or no information on the material and/or optical properties of the satellite surfaces, mostly because the wire-frame models are typically based on single spectral band imaging data. Detailed surface material and property characterization requires multi-band photometric and/or spectrometric measurements.

3 INVERSION FORMULATION

The analysis can be formulated as an inversion problem that requires three main types of input information: 1) a wireframe (i.e., shape) model of the observed satellite, 2) an attitude model for the satellite, and 3) a series of non-resolved multi-band or spectrometric brightness measurements of the satellite reflecting sunlight. The first two of these can be derived through a variety of means, including open-source publications or analysis of resolved imagery of the satellite (either pre-launch or on-orbit). The second input might comprise visible and near-IR spectra from a ground-based long-slit spectrograph system. This would provide measurements of the distribution of reflected sunlight as a function of wavelength, which would naturally contain an abundance of information on the material-specific reflective properties of the satellite surfaces. However, such spectrometric instruments often provide brightness measurements of *the entire object*, rather than from individual satellite surfaces or component. In other words, each measurement represents a summation of light reflected from many satellite surfaces, thereby requiring an inversion process to separate and retrieve individual surface properties. This paper describes the theory and details of such an inversion method.

3.1 Satellite Wireframe Shape Models

Several sophisticated software tools have been developed to exploit resolved imagery of satellites. These models are typically assembled from primitive components (such as flat panels, cylinders, cones, parabolic dishes, etc.) which can be combined to form accurate three-dimensional representations of the satellite. Fig. 1 illustrates the software analysis process for optical imagery. The analysis process essentially translates the two-dimensional imagery into detailed three-dimensional information about the sizes, shapes, and relative orientations of various spacecraft surfaces. Performing this process for a series of many images also yields a model of the attitude profile of the satellite (i.e., the body orientation as a function of time). Taken as a whole, the imagery data analysis allows analysts to assemble a wire-frame shape model and an attitude model for the satellite.

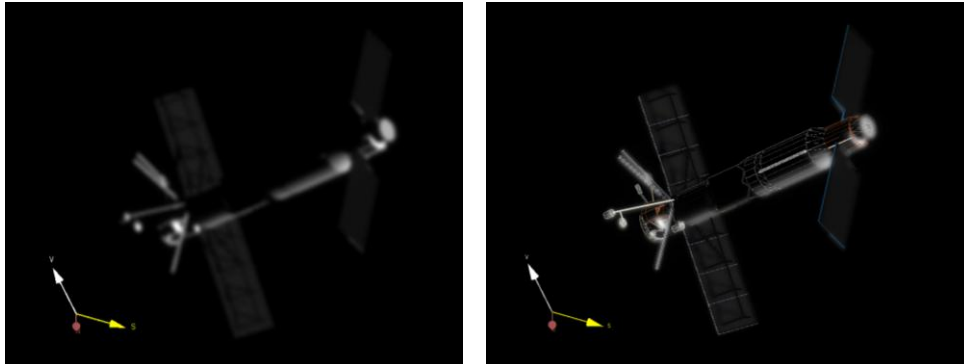


Fig. 1. Simulated telescopic visible-band image frame of SeaSat satellite (left panel) along with a wire-frame model aligned and over-plotted (right panel). Similar analysis of many sequential frames provides the means to translate the two-dimensional image data into detailed three-dimensional information, including the shape of the satellite (i.e., the properly-sized wire-frame model) as well as its attitude (i.e., the body orientation as a function of time).

After such model development is complete, each component of the wire-frame model can be decomposed into a series of perfectly flat facets spanning the various surfaces of the satellite. Notably, even round components (such as the cylinders and parabolic dishes shown in Fig. 1) may be approximated in this manner, even though they may require many small facets. Each resultant facet may be described as a planar polygon with shape, area, and orientation derived from the original wire-frame model.

3.2 Satellite Attitude Models

Analysis of high-quality images also indicates the orientation of the spacecraft as a function of time, derived from the sequential frame-to-frame adjustments required to align the wire-frame model to the series of observed images. For stabilized satellites, this frame-to-frame orientation data can be used to construct a

complete attitude model, which can be described using typical spacecraft attitude control system (ACS) terms. For instance, many actively stabilized satellites maintain a “nadir-velocity” attitude profile, where the ACS maintains one of the spacecraft body axes pointed towards the nadir direction, and another body axis pointed as much as possible into the direction of motion. Other stabilization modes also are common (e.g., “nadir-solar,” “ECI-fixed,” and spin-stabilized attitude profiles). Detailed image analysis can reveal such ACS operational modes, or, alternatively, indicate the rotation-state parameters for spin-stabilized satellites or even for tumbling objects. Ultimately, this information can be used to assemble an “attitude model”, used to specify the body’s orientation at the time of each multi-band measurement to be used in the inversion process. Additionally, other sources of information could be used to construct, confirm or enhance such an attitude model, such as open-source publication ACS operational parameters, or information provided by the satellite’s owner.

In mathematical terms, the attitude model comprises the set of all parameters required to specify the body’s “attitude matrix,” \mathbf{R} , as a function of time. This 3×3 rotation matrix converts vectors from an inertial reference frame (taken here to be the Earth-centered J2000 frame) into the body-fixed reference frame, and can be written symbolically as follows:

$$\mathbf{R} = \mathbf{R}(t) \tag{1}$$

where the time dependence indicates the changing orientation of the satellite. As an example, the attitude matrix provides the means to convert the satellite-to-observer unit direction vector in the inertial reference frame, $\mathbf{o}^*(t)$, into a body-frame vector through matrix multiplication as follows:

$$\mathbf{o}(t) = \mathbf{R}(t) \mathbf{o}^*(t) \tag{2}$$

In this discussion, the “*” superscript denotes inertial frame vectors and body-frame vectors are denoted without superscripts. The satellite-to-Sun inertial unit direction vector can be similarly written:

$$\mathbf{s}(t) = \mathbf{R}(t) \mathbf{s}^*(t) \tag{3}$$

The two vectors given in Eqs. (3) and (4) play an important role in determining the observed brightness of sunlight reflected from the body, as described below. While both of these vectors depend on time, in this discussion their explicit time dependence will often be suppressed for brevity.

A high-fidelity attitude model derived from a sequence of images often provides a means of reliably predicting the orientation of the satellite at times well beyond the original imaging observations. In other words, the matrix $\mathbf{R}(t)$ can be calculated at the times of any future observations, allowing the body-frame $\mathbf{o}(t)$ and $\mathbf{s}(t)$ vectors to be calculated for those times as well. This means that the spectrometric observations used for surface characterization need not be simultaneous with the imagery used to construct the attitude model. As will become apparent from the inversion theory developed in the next section, there really is no requirement on exactly when the multi-band observations are conducted, as long as the satellite attitude model provides valid satellite orientations at the time of each measurement.

3.3 Theory of Satellite Surface Characterization using Multi-band Observations

The satellite wire-frame and attitude models described above provide a means of calculating the visibility and observation geometry of each resolved spacecraft surface during follow-up observations from any multi-band sensor with a known location. Notably, if one also had detailed *a priori* knowledge of the optical properties of each surface — i.e., the material composition, and associated bi-directional reflectance distribution function (BRDF) — then a forward model of the spectral signature of the entire body could be constructed by summing the contributions over all of the surfaces visible to the sensor. However, in the absence of such *a priori* knowledge, characterizing the surface properties requires an inversion of the multi-band measurements. Ideally, these measurements would be obtained by spectrometric instrumentation with good spectral resolution and a good temporal cadence. This would provide an abundance of spectral diversity to identify different surface materials with the least ambiguity. However,

the task could also conceivably be performed by a multi-channel photometer instrument providing relatively broad-band spectral coverage.

3.3.1 The Spectral Intensity of a Satellite Reflecting Sunlight

The satellite wire-frame models provide the orientation and area of each facet of each satellite component, information essential to the inversion process. Specifically, the k^{th} facet of the j^{th} component may be characterized by its surface area, $A_{j,k}$, and normal unit vector, $\mathbf{n}_{j,k}$. These facets could, in principle, have time dependent orientations, $\mathbf{n}_{j,k}(t)$, such as articulating spacecraft structures, but this potential time dependence will be suppressed here for brevity. The spectral intensity (or spectral radiance), L , of sunlight reflected from the entire object has units of $\text{W ster}^{-1} \mu\text{m}^{-1}$. It is a function of both time and wavelength, and may be expressed as a summation over the component facets:

$$L(t, \lambda) = F_{\text{Sun}}(t, \lambda) \left\{ \sum_{j,k} A_{j,k} \langle \mathbf{n}_{j,k} \cdot \mathbf{o} \rangle \langle \mathbf{n}_{j,k} \cdot \mathbf{s} \rangle \rho_j(\lambda, \mathbf{n}_{j,k}, \mathbf{o}, \mathbf{s}) \Psi_{j,k}(\mathbf{o}, \mathbf{s}) \right\} \quad (4)$$

where $F_{\text{Sun}}(t, \lambda)$ denotes the illuminating solar irradiance ($\text{W m}^{-2} \mu\text{m}^{-1}$), \mathbf{o} and \mathbf{s} denote the time-dependent satellite-to-observer and satellite-to-Sun unit vectors from Eqs. (2) and (3), and the function $\rho_j(\lambda, \mathbf{n}, \mathbf{o}, \mathbf{s})$ denotes the surface BRDF for satellite component j . Angular brackets denote the non-negative operator:

$$\langle x \rangle \equiv \begin{cases} x & x \geq 0 \\ 0 & x < 0 \end{cases} \quad (5)$$

and the non-negative dot products in Eq. (4) ensure that contributions arise only from facets showing an illuminated side to the observer. The shadowing/masking function, $\Psi_{j,k}(\mathbf{o}, \mathbf{s})$, denotes the fraction of each facet that is *not shadowed nor obscured* by other satellite surfaces. For convex bodies $\Psi_{j,k} = 1$ for all facets. For non-convex bodies this function generally varies with time. The relative positions and sizes of the satellite components specified in the wire-frame model, combined with the \mathbf{o} and \mathbf{s} vectors, provide a means to calculate this function using ray-tracing, z-buffering, or similar algorithms.

Notably, the satellite wire-frame and attitude models together provide all of the quantities required to calculate the spectral intensity using Eq. (4) except for knowledge of the surface bi-directional reflectance distribution functions, or BRDFs. In fact, the importance of the wavelength-dependent BRDF in Eq. (4) cannot be overemphasized in this regard. It basically indicates how reflectance spectroscopy can be used to diagnose the material composition of individual surfaces, and is fundamental to the feasibility of the inversion process. Because the whole-satellite spectral intensity in Eq. (4) represents a summation over all satellite surfaces, the main thrust of this research program entails formulating a procedure to separate and retrieve the *individual* surface properties.

Many groups have measured material BRDFs in laboratory environments and/or created numerical BRDF models. For instance, BRDFs for several spacecraft materials — such as solar array panels, milled aluminum, anodized aluminum, multi-layer insulation, white paint, etc. — are available as part of the TASAT signature simulation software package [1]. Many of these show tell-tale spectral features that can be used as “fingerprints” to identify the material composition of satellite surfaces in solar reflectance spectra [2, 3]. BRDFs for different materials also vary significantly in their relative fractions of specular vs. diffuse reflectance. A robust inversion method should exploit both of these aspects of BRDFs for surface material characterization. In particular, the formulation presented here focuses on how a database of candidate materials, along with their laboratory-measured or modeled BRDFs, can be used in an inversion analysis in order to derive corresponding material abundances covering the various spacecraft components.

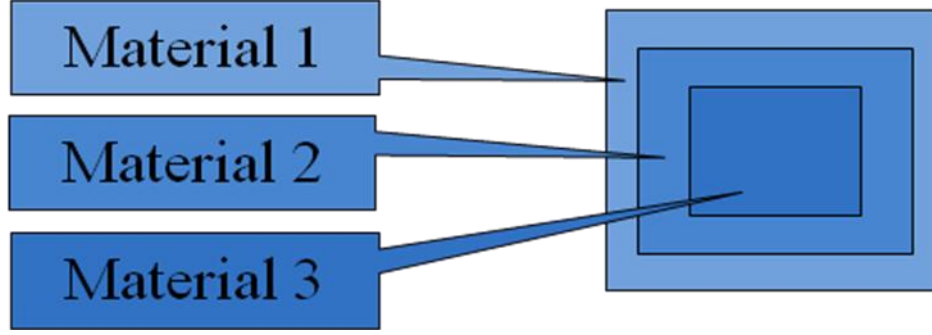


Fig. 2. The multi-material composition model illustrating the assumption that each resolvable satellite component — such as the cylinders, panels, and parabolic dishes in the wire-frame model shown in Fig. 1 — can be decomposed into an areal mixture of distinct materials. For instance, a solar power panel might consist of solar array material (material 3) encased in an aluminum frame (material 2) surrounded by insulation material (material 1).

3.3.2 Spectral Intensity Inversion Theory using Laboratory-Measured Material BRDFs

As a first step, this formulation assumes that the surfaces of each resolvable component in the satellite shape model can be decomposed into a set of distinct materials, as illustrated in Fig. 2. In this case, the *effective* BRDF for the k^{th} facet of the j^{th} satellite component may be written as a sum over the individual material BRDFs as follows:

$$\rho_j(\lambda, \mathbf{n}_{j,k}, \mathbf{o}, \mathbf{s}) = \sum_m f_{j,m} \beta_m(\lambda, \mathbf{n}_{j,k}, \mathbf{o}, \mathbf{s}) \quad (6)$$

where $f_{j,m}$ denotes the fractional area of component j covered by material m , and $\beta_m(\lambda, \mathbf{n}, \mathbf{o}, \mathbf{s})$ denotes the BRDF for the pure material m . Inserting Eq. (6) into Eq. (4) and re-arranging yields:

$$L(t, \lambda) = \sum_{j,m} f_{j,m} K_{j,m}(t, \lambda) \quad (7)$$

where the kernel is

$$K_{j,m}(t, \lambda) = F_{\text{Sun}}(t, \lambda) \left\{ \sum_k A_{j,k} \langle \mathbf{n}_{j,k} \cdot \mathbf{o} \rangle \langle \mathbf{n}_{j,k} \cdot \mathbf{s} \rangle \beta_m(\lambda, \mathbf{n}_{j,k}, \mathbf{o}, \mathbf{s}) \Psi_{j,k}(\mathbf{o}, \mathbf{s}) \right\} \quad (8)$$

Notably, all the quantities in the kernel are known from either independent measurement (such as the solar flux and the database of laboratory-measured BRDFs) or from the wire-frame and attitude models. The only remaining unknown quantities are the fractional areas covered by the pure materials, $f_{j,m}$. These quantities are subject to the following constraints:

$$0 \leq f_{j,m} \leq 1 \quad (9)$$

$$\sum_m f_{j,m} = 1 \quad (10)$$

The objective of the inversion process is to find the set of fractional areas, $f_{j,m}$, that best reproduce the observed spectral radiance data but that also satisfy these two constraints.

Typical long-slit spectrographs or broad-band photometric instruments do not provide continuous measurements of the spectral intensity, $L(t, \lambda)$, but instead provide observations at a discrete set of times,

$\{t_i, i=1\dots N_i\}$ and wavelengths, $\{\lambda_l, l=1\dots N_l\}$. This formulation idealizes each of these measurements as instantaneous (i.e., neglecting the finite exposure time spanned by each spectral measurement) with perfectly narrow wavelength sampling (i.e., neglecting the finite width of each spectral channel). With these assumptions, the spectrometric measurements can be organized into a discrete matrix as follows:

$$L_{i,l} = L(t_i, \lambda_l) \quad (11)$$

and Eq. (7) can be used to write the system of equations that must be solved in the inversion process

$$L_{i,l} = \sum_{j,m} f_{j,m} K_{i,l,j,m} \quad (12)$$

At this point it is convenient to combine indices to streamline the formulation. The two observation indices (i, l) can be combined into one master index, μ , which spans the range from $\mu = 1 \dots N_i N_l$. Similarly, the indices (j, m) can be combined into master index ν . Using these master indices, Eq. (12) can be re-written in a relatively simple form:

$$L_{\mu} = \sum_{\nu} f_{\nu} K_{\mu,\nu} \quad (13)$$

At first glance, Eq. (13) appears to be a linear system which could be solved using a variety of methods such as singular-value decomposition or using the pseudo-inverse matrix formalism [4]. However, the constraints stated in Eqs. (9) and (10) still must be satisfied, making such methods inappropriate. Fortunately, there are efficient numerical methods that do provide a means of imposing such constraints [5, 6]. Solving Eq. (13) using such methods provides the set of f_{ν} or, alternatively, $f_{j,m}$, which represent the inverted fractional areas of each satellite component covered by each reflective material.

In the idealized case where the j^{th} component is *actually* covered with material m' , then the solution to Eq. (13) should yield Kronecker's delta-function, $f_{j,m} = \delta_{m,m'}$. However, for real-world cases, a combination of incomplete observations, measurement uncertainties, inadequately characterized BRDFs, and an incomplete materials database will likely lead to departures from such idealized solutions. For instance, if a satellite component were actually covered with white-paint, but the only constraining spectral measurements were relatively noisy, then the inversion solution may indicate white paint as a dominant component, as well as significant but erroneous contributions from other materials included just to improve the fit to the noisy data.

4 APPLICATION TO SIMULATED OBSERVATIONS OF A CUBICAL SATELLITE

This section applies the inversion method to simulated observations of a relatively simple cubical satellite, providing a convenient means of testing and validating both the formulation and software implementation. Because a cube is a convex shape, it also obviates the need to calculate the shadowing/masking function.

4.1 Cubical Satellite Parameters

The cube used in the simulations measures 10 cm per side. Each face represents a different “component” of the satellite (i.e., $j = 1 \dots 6$), with each composed of a different material. Simulated spectral intensities were calculated using Eqs. (7) and (8), with materials and BRDFs taken from the TASAT database [1]. Table 1 lists the six materials covering the cube's faces, and the associated BRDF parameters. Fig. 3 shows plots illustrating these six BRDFs, illustrating two important aspects of material BRDFs: 1) the relative strength of specular vs. diffuse reflection components (shown in the top panels), and 2) the wavelength dependence of the total hemispherical reflectance (shown in the bottom panels). The inversion method outlined here is sensitive to both of these aspects of material reflectance.

Component Index, j	Cube Face	BRDF Type	BRDF Number	Material Description, finish and other details
1	+x	Maxwell Beard	0046	Aluminum Alloy, 5456-H116, Mill Finish
2	+y	Maxwell Beard	0020	Paint, Chemglaze A276, White
3	+z	Maxwell Beard	0029	Mylar, Aluminized, Mylar Side
4	-y	Maxwell Beard	0084	Solar Cell, Stack, Sun Side
5	-z	Phong	0087	Paint, Chemglaze Z754, Blue
6	-x	Maxwell Beard	0021	Paint, Chemglaze A382, Black

Table 1. Materials and BRDFs used for the six cube faces in the spectral radiance simulations.

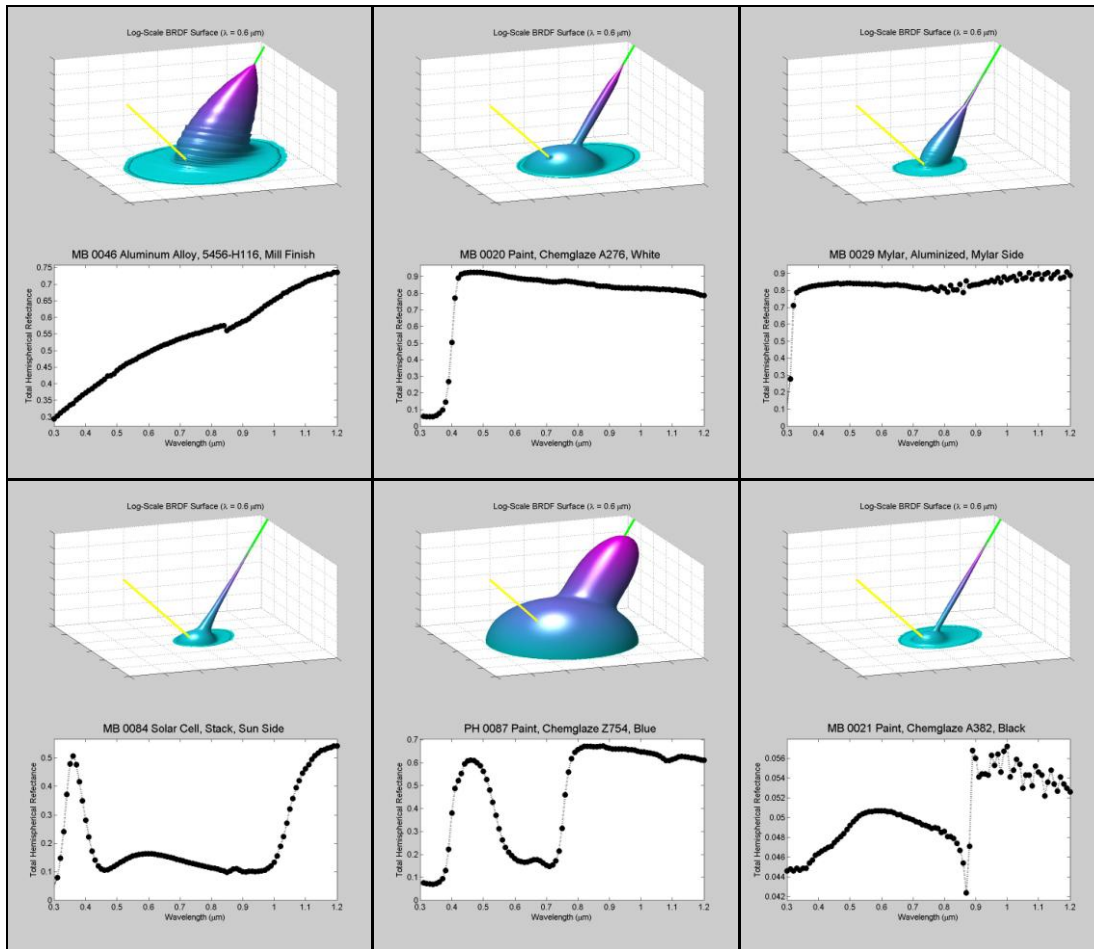


Fig. 3. BRDF plots for the six cube face materials listed in Table 1. The top panels show surface representations of each BRDF at a wavelength of $\lambda = 0.6 \mu\text{m}$, illustrating the specular and diffuse reflection components. The yellow line in these plots indicates an example incident illumination direction, and the green line the corresponding direction of specular (i.e., mirror-like) reflection. Shiny materials have BRDFs with long and sharp spikes along this green line. The bottom panels plot the total hemispherical reflectance as a function of wavelength over the range $0.3 \leq \lambda \leq 1.2 \mu\text{m}$, indicating the color of the material.

4.2 Inversion Results for Laboratory-Style Scans

Two basic types of simulations were used to test the inversion process. The first “laboratory-style scans” comprise the kind of measurements that might be performed in a laboratory environment, where an object

is mounted on a spinning turn-table and viewed or illuminated from a variety of directions. These types of simulations will be described in this section. The second category, simulations of an object in orbit as observed by ground-based sensors, will be described in the next section.

Fig. 4 shows several still-frame plots from an animated representation of a laboratory-style scan of the cube described above. Each frame shows two plots of the brightness for wavelength $\lambda = 0.8 \mu\text{m}$ (approximately the astronomical I-band). The top plots show the brightness in terms of optical cross section, OCS , which is the spectral intensity divided by the illuminating solar flux

$$OCS(t, \lambda) = \frac{L(t, \lambda)}{F_{\text{Sun}}(t, \lambda)} \quad (14)$$

The bottom plots show the I-band stellar magnitude (normalized to an object range of 1000 km), which is just a logarithmic measure of the OCS . The scan shown in Fig. 4 spans two minutes of time with a sampling rate of 1 Hz. It is a “complete” scan, in that it provides views of all six sides of the cube in reflected light.

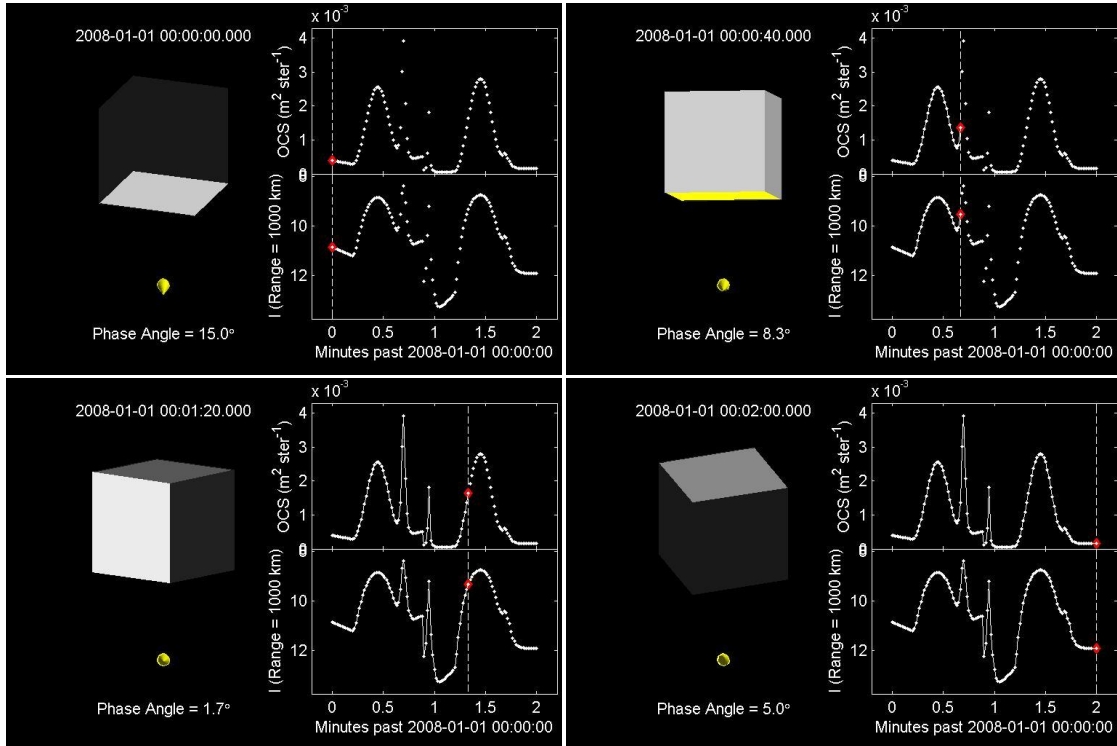


Fig. 4. Still-frame plots from an animated representation of a complete, noise-free laboratory-style scan of the cube. Each frame illustrates a single time-step of the two-minute scan, with a rendering of the illuminated cube as seen from the sensor’s vantage point (upper left), the illumination direction and phase angle (lower left), the optical cross section (upper right) and the range-normalized stellar magnitude (lower right). Faces of the cube reflecting light in a strong specular fashion are rendered in yellow. The OCS and magnitude signatures in these plots correspond to light reflected at a wavelength of $\lambda = 0.8 \mu\text{m}$.

Fig. 4 shows brightness plots for one wavelength, $\lambda = 0.8 \mu\text{m}$. As mentioned previously, the inversion process relies on having multi-band data, so the actual tests of the method discussed here employ simulated brightnesses at ten wavelengths: 0.2, 0.4, 0.6, 0.8, 1.0, and 1.2 μm . Fig. 5 shows multi-band OCS surface plots for the same two-minute scan sampled at 1 Hz, for a noise-free case (left) and with 10% additive

Gaussian noise (right). Each vertex on these surfaces represents a data-point employed in the inversion analyses described below.

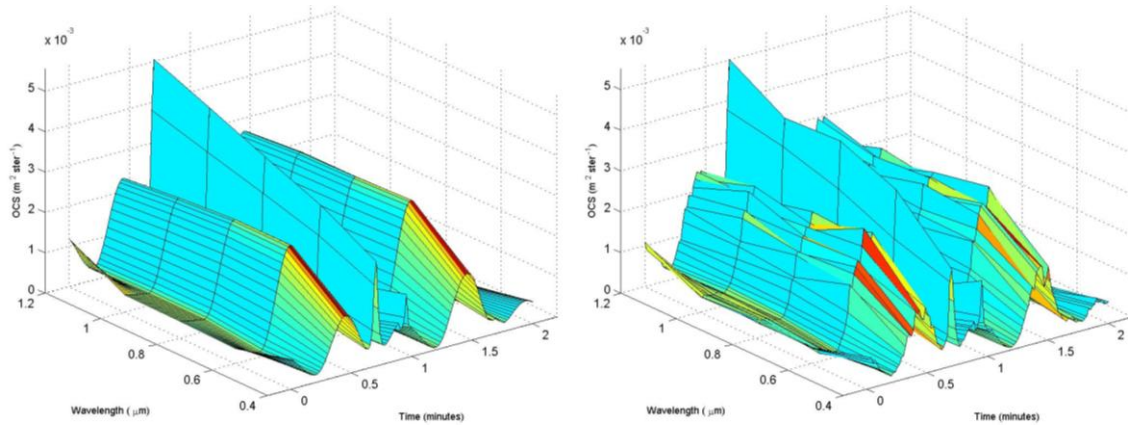


Fig. 5. Surface plots of simulated multi-band optical cross sections for a two-minute laboratory-style scan of the cube with a sampling rate of 1 Hz. The left panel shows the noise-free OCS values, and the right panel shows OCS values corrupted by 10% Gaussian noise.

4.2.1 *Noise-free Complete Scan (Truth Retrieval)*

Retrieving the exact inputs for a noise-free simulation represents a reasonable first test for any inversion analysis. Fig. 6 illustrates such a “truth retrieval” analysis for the complete, noise-free cube scans shown in Fig. 4 and the left panel of Fig. 5. For this test, the list of candidate materials comprised the exact same six actually used for the faces of the cubes ($m = 1 \dots 6$). The plot in Fig. 6 shows a color representation of the material fractions, $f_{j,m}$, calculated by the inversion process. The distinctive pattern of $f_{j,m} = 1$ along the diagonal and $f_{j,m} = 0$ elsewhere, represents a retrieval of known truth — a validation of the theory and implementation of the inversion method.

4.2.2 *The Effect of Superfluous Materials*

Fig. 7 illustrates another inversion analysis using the same noise-free input data as in the previous example. However, this test employs twelve candidate materials ($m = 1 \dots 12$): the six used for cube faces *plus* an additional six not used anywhere on the cube. Fig. 7 shows a color representation of the material fractions, $f_{j,m}$, calculated in this case. The diagonal pattern on the left hand side of the plot represents successful truth retrieval, even in the presence of the six superfluous candidate surface materials.

4.2.3 *The Effect of Measurement Noise*

Fig. 8 illustrates a similar inversion analysis as in the previous example, but modified to employ the noisy multi-band data shown in right panel of Fig. 5. In this case, the nearly diagonal pattern on the left side of the plot represents a successful but imperfect truth retrieval. The non-zero fractions seen off of the diagonal indicate the effects of noise on the inversion process, where erroneous contributions from other materials were included just to improve the fit to the noisy data.

4.2.4 *The Effect of Unknown or Excluded Materials*

Fig. 9 illustrates a similar inversion analysis as in the previous example, but modified so that one of the materials actually on the cube is excluded from the list of candidate materials. Specifically, the solar-cell material covering the +y face, “Solar Cell, Stack, Sun Side”, has been excluded from the candidate list and substituted with an alternate material. In this case, the process cannot retrieve the truth even for noise-free input data, because the actual material for the +y face is not even included among the candidates. The inversion indicates that the best fit for the -y face is a mixture of two alternate solar panel materials: roughly 85% “Solar Cell, Silicon, BFSR, Sun Side” plus 15% “Solar Cell, Silicon, CC Blue, Sun Side” with negligible fractions of other materials. The implication is that, when confronted with an unknown

material, the inversion process substitutes a weighted combination of other, similar candidate materials. Notably, Fig. 9 indicates that the quality of retrieval for the +z face suffered in this case, even though its actual material was included on the candidate list. This indicates that incomplete or imperfect candidate material databases can affect the quality of retrieval for various components around the whole-body, regardless if their materials contained in the database or not. This result could represent a fundamental limitation of the method; it deserves further investigation because spacecraft material databases are notoriously incomplete, and this effect may not be uncommon in real-world applications.

4.2.5 The Effect of an Incomplete Scan

Fig. 10 illustrates a similar inversion analysis as in the previous example, but modified to an *incomplete* noise-free scan of the cube. The scan is incomplete in that it fails to detect light reflected from either the top (+z) or the bottom (-z) faces of the cube. In this case, the inversion process simply cannot determine any material fractions for those two components of the satellite. The plot in Fig. 10 illustrates this effect by showing two rows in black, corresponding to these undetected faces. These black vs. non-black regions comprise a “detectability” map for the inversion, indicating at a glance which satellite components have been detected in the multi-band observations. Notably, however, the faces that were detected in this noise-free scan show the diagonal pattern of perfect truth retrieval.

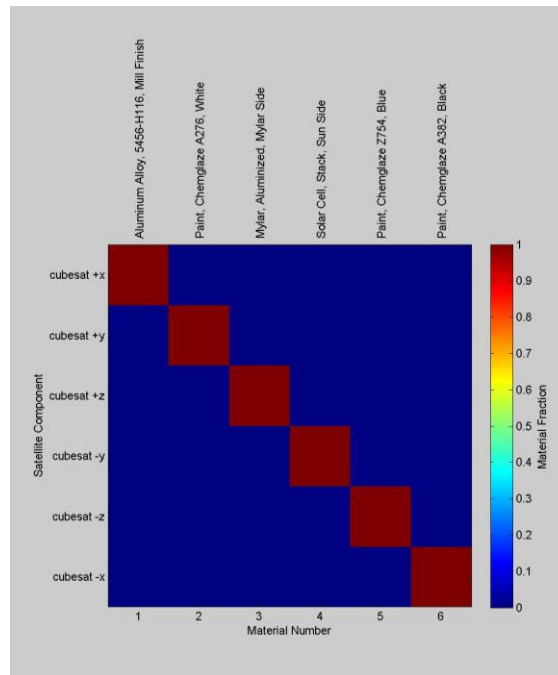


Fig. 6. Inverted material area fractions, $f_{j,m}$, for a complete, noise-free scan of the cube. The six satellite components (i.e, faces) are listed along the vertical axis and the six candidate materials along the horizontal axis. The distinctive diagonal pattern of the fractions ($f_{j,m} = 1$ along the diagonal and $f_{j,m} = 0$ elsewhere) represents truth retrieval, i.e., a perfect reproduction of the known input.

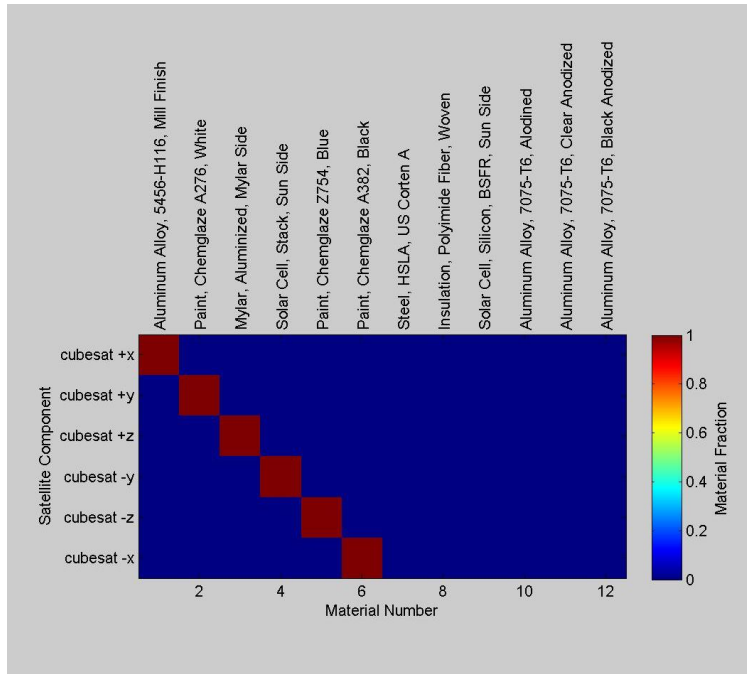


Fig. 7. Inverted material area fractions, $f_{j,m}$, for a complete, noise-free scan of the cube using twelve candidate materials, the six actually used on the cube plus another set of six materials not used anywhere on the cube. The diagonal pattern of the fractions on the left side of the plot represents a successful retrieval of the known truth, even in the presence of such superfluous candidate materials.

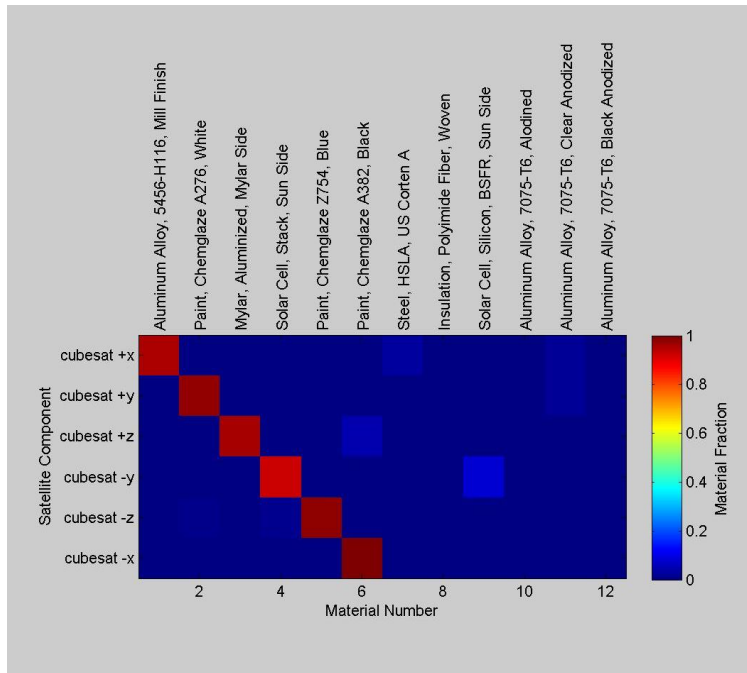


Fig. 8. Inverted material area fractions, $f_{j,m}$, for a complete but noisy scan of the cube. The nearly diagonal pattern of the fractions on the left side of the plot represents a successful but imperfect retrieval of known truth.

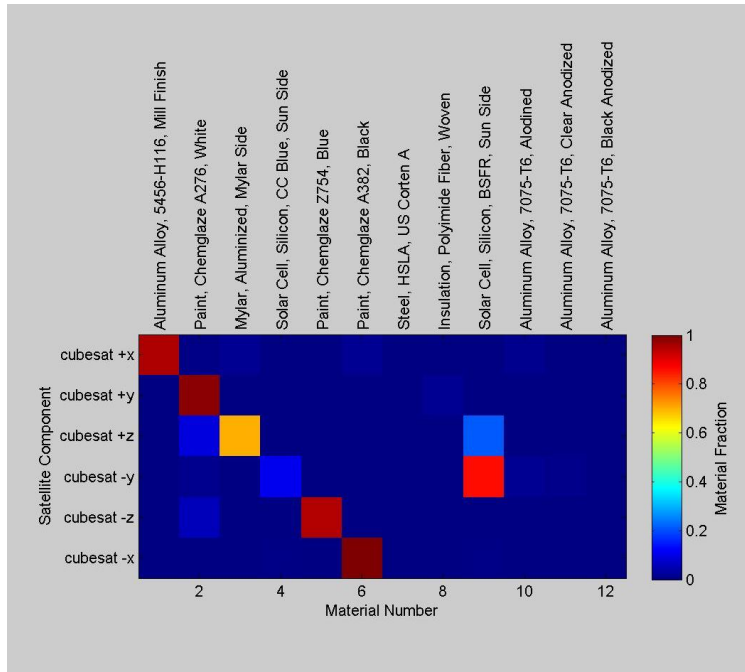


Fig. 9. Inverted material area fractions, $f_{j,m}$, for a complete but noisy scan of the cube where one of the actual face materials is unknown. In this case, the candidate list excludes the material actually used for the $-y$ face. The roughly diagonal pattern on the left side of the plot represents the best retrieval possible when confronted with such an unknown material.

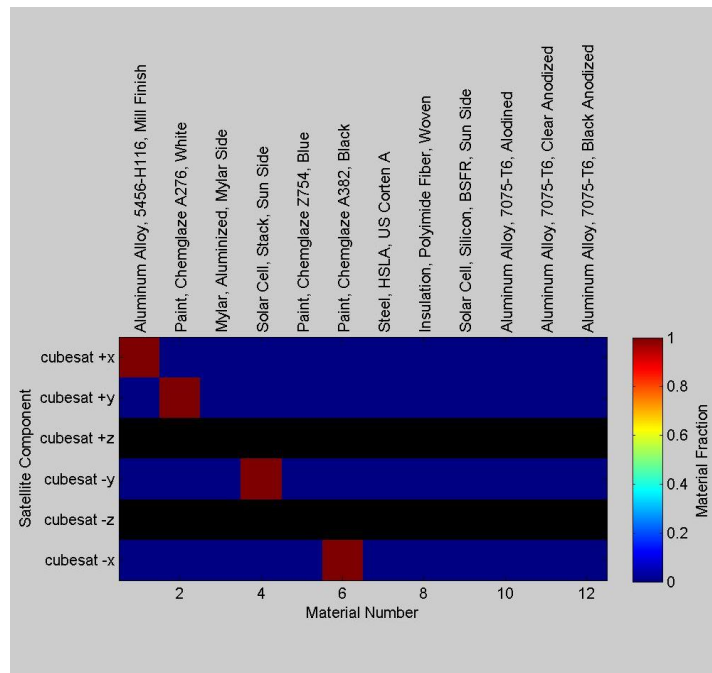


Fig. 10. Inverted material area fractions, $f_{j,m}$, for an incomplete, noise-free scan of the cube. In this case, the limited laboratory scan failed to detect light reflected from the top (+z) or the bottom (-z) cube faces. The plot shows these undetected components as black rows, creating a “detectability” map for the inversion. Notably, the detected faces show the diagonal pattern of perfect truth retrieval.

4.3 Inversion Results for Ground-Based Observations

The lessons learned from the simulations of the laboratory-style scans discussed above are valuable in understanding the inversions for objects in orbit as observed by ground-based sensors. For instance, it is common that ground-based observations do not detect reflection from extensive sections of real satellites, even when conducted from multiple sites over extended time periods. For instance, ground-based observations of a nadir/velocity stabilized satellite in low-Earth orbit (LEO) simply cannot detect any light reflected from surfaces facing towards the zenith (i.e., anti-nadir) direction. So the “detectability map” introduced earlier is key in interpreting results for real satellites.

Fig. 11 shows three frames from an animation of a simulated ground-based observation of the same 10cm cube flying in the orbit of the LEO satellite SSN 22176. The simulation assumes nadir/velocity stabilization, with the cube’s +z face continuously facing nadir and the +x face facing towards the velocity vector. The plots in Fig. 11 show renderings of the cube (upper right), its position along the ground-track (upper left) and the I-band ($\lambda = 0.8 \mu\text{m}$) brightness detected by the AMOS observatory sampled with a cadence of once every 15 s (assuming 10% Gaussian noise). During the 25 minute duration of this 2009 Jan 01 pass, the simulations indicate that AMOS observatory detects sunlight reflected from three of the cube’s sides.

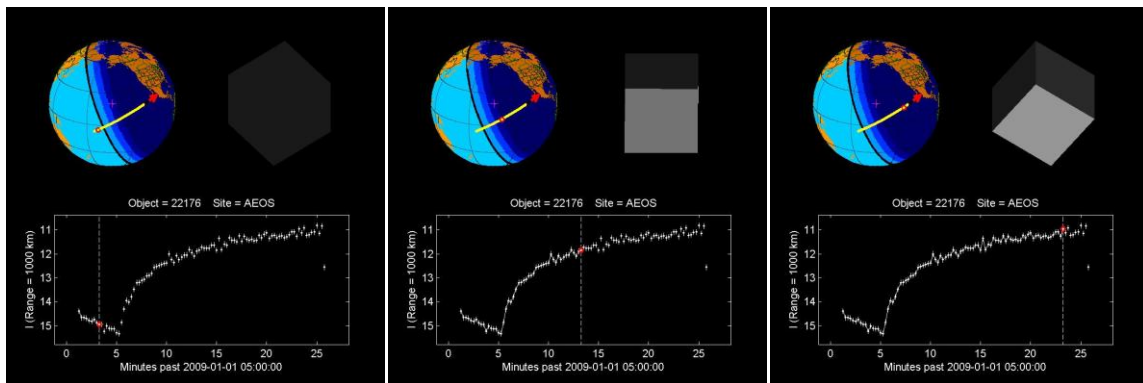


Fig. 11. Three frames from an animation of a simulated ground-based observation of the cube flying in the orbit of SSN 22176 making a pass over AMOS on 2009 Jan 01. The simulation assumes nadir/velocity stabilization, with the +z face continuously facing nadir and the +x face towards the velocity vector. Each plots shows a single time-step in the simulation, with renderings of the cube reflecting sunlight (upper right), its position along the ground-track (upper left) and the whole-body I-band ($\lambda = 0.8 \mu\text{m}$) brightness in range-normalized stellar magnitudes (lower panel). The simulation assumes 10% Gaussian noise on the brightness measurements.

To demonstrate the effects of multi-site observations, the inversions discussed here employ observations from a total of three passes acquired from two ground-based sites. The first pass occurred over the SOR observatory in New Mexico beginning at about 2009 Jan 01 0300 UT. The next two occurred over AMOS later that day beginning at about 0500 UT (this is the pass shown in Fig. 11) and another at about 1500 UT. The top panels of Fig. 12 show the ground-tracks for these three passes, and the middle panels show the associated simulated multi-band *OCS* values (sampled once every 15 s for wavelengths 0.2, 0.4, 0.6, 0.8, 1.0, and 1.2 μm) used as input to the inversion process. The lower panels in Fig. 12 show inversion results in the same format used for Fig. 6 through 10. However, these lower panels show the *cumulative* inversion results: the leftmost shows the inversion for the first pass alone, the middle for the first two passes combined and the rightmost for all three passes combined. These cumulative results illustrate two effects: 1) the accuracy of the process grows with increased quantities of multi-band data, and 2) additional passes tend to reveal more and more of the satellite’s components. Specifically this latter effect is apparent in that the third pass provides inversion results for the +x face of the cube, which had not been detected in the previous two passes. Given a comprehensive, multi-perspective set of observations (including both ground-based and space-based sensors, for instance), one would expect these plots to approach those shown

in Fig. 7 or 8, as more and more components are revealed and the inverted material fractions converge to the diagonal pattern of known truth.

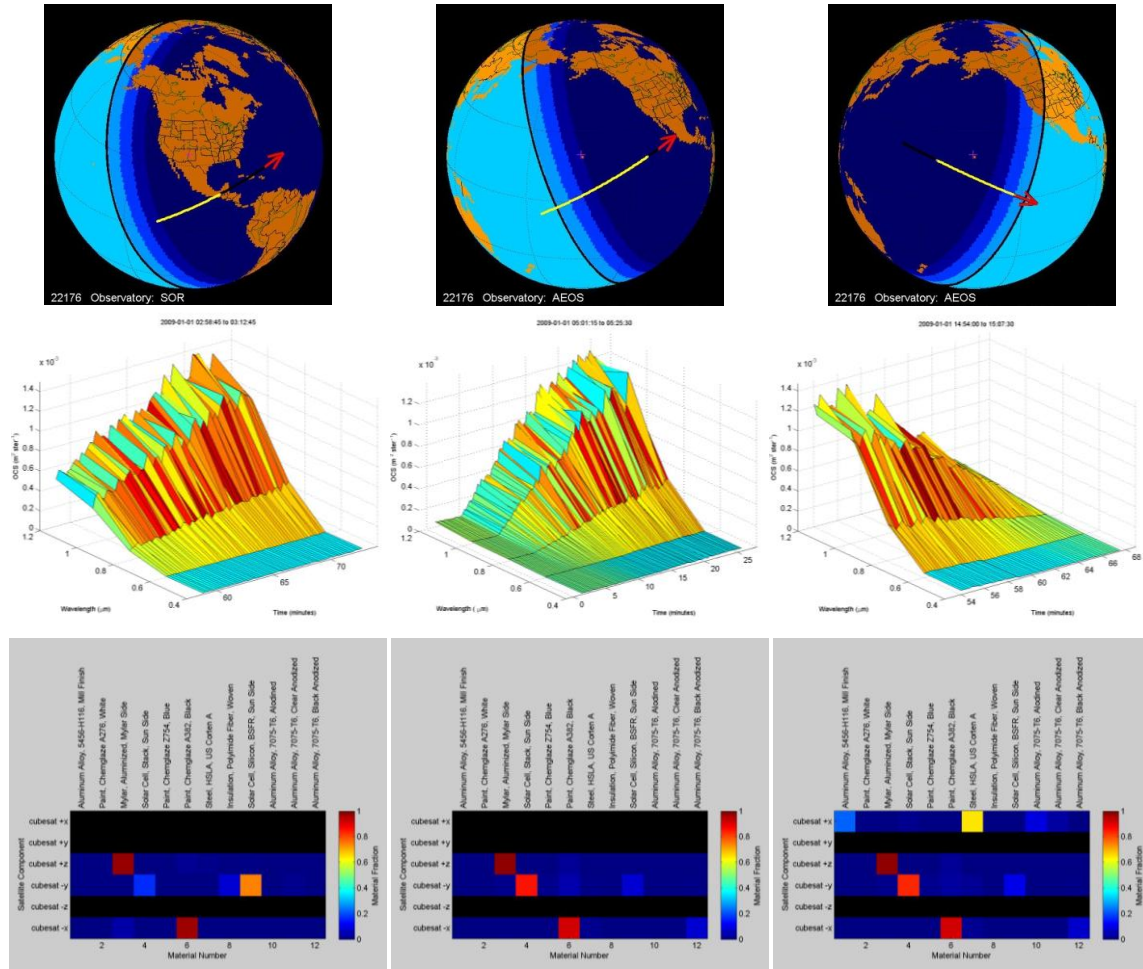


Fig. 12. The three simulated passes and results for inversion of the cube observed from ground-based sensors. The top panels show the ground-tracks of the passes: the first pass occurred over SOR in New Mexico beginning at about 2009 Jan 01 0300 UT and next two over AMOS later that day at about 0500 UT and 1500 UT. The middle panels show the associated multi-band OCS values for each pass, used as input to the inversion process. The lower panels show the inverted material area fractions, $f_{j,m}$. Note these lower panels show the *cumulative* results: the leftmost plots the $f_{j,m}$ values for the first pass alone, the middle for the first two passes combined, and the rightmost for all three passes combined.

5 CONCLUSIONS AND FUTURE WORK

Satellite surface materials and abundances can be estimated from temporal sequences of whole-body multi-band brightness measurements via an inversion analysis process. The process requires the following as input: 1) a set of multi-band measurements of a satellite's whole-body reflected-sunlight brightness, 2) the satellite's wire-frame model, including each major component capable of reflecting sunlight, 3) the satellite's attitude, specifying the body's orientation at the time of each multi-band measurement, and 4) a database of bi-directional reflection distribution functions for a set of candidate surface materials. As output, the inversion process yields estimates of the fraction of each satellite component covered by each candidate material. Analyses of simulated multi-band observations of a cubical satellite provides a simple and convenient means of testing and verifying the software implementation, as well as learning the expected outcomes for actual satellites. Tests conducted so far include simulations of both laboratory-style

scans and multi-site ground-based observations of a 10 cm cubical satellite with faces composed of six different materials. The inversion method successfully retrieves the six surface materials for a complete noise-free scan of the cube. It also performs reasonably well when confronted with the effects of measurement noise, superfluous or unknown materials, and incomplete observations — adversities expected for any realistic real-world application.

To extend the inversion effort, future tests and analyses will include the following tasks:

1. Implement methods of estimating uncertainties of the inverted material fractions.
2. Apply the method to simulations of more complex satellites with concavities and a larger suite of surface materials.
3. Account for the finite exposure durations of spectrometric measurements.
4. Account for the finite spectral width of spectrometric channels and/or broad-band photometric response functions.
5. Implement algorithms to allow combining data from different sensors, like a high-resolution spectrograph at one ground-based observatory with a multi-channel broad-band photometer located at another.
6. Implement a linear-programming algorithm to find the best *single* material associated with each satellite component, rather than the best mixture of materials presented here.
7. Investigate the possibility of retrieving material BRDF parameters themselves from multi-band observations, rather than using a material database as input, to enable the characterization of completely unknown materials and to study the effects of space weathering.

6 REFERENCES

1. Riker, J., and Butts, R., "The Time-Domain Analysis Simulation for Advanced Tracking (TASAT) Approaches to Compensated Imaging", SPIE Vol.1688, *Atmospheric Propagation and Remote Sensing*, 1992.
2. Jorgensen, K., "Using Reflectance Spectroscopy to Determine Material Type of Orbital Debris", Ph.D. Thesis, Univ. of Colorado, Boulder, May 2000.
3. Jorgensen, K., Okada, J., Guyote, M., Africano, J., Hall, D., Hamada, K., Barker, E., Stansbery, G., and Kervin, P., "Reflectance Spectra of Human-made Objects", *2004 AMOS Technical Conference*, Wailea, Maui, Hawaii, 13 –17 September 2004.
4. Press, W. et. al., "Numerical Recipes in FORTRAN: The Art of Scientific Computing" (2nd Edition), Cambridge University Press, New York NY, 1992.
5. Lawson, C. and Hanson, R., "Solving Least Squares Problems" Prentice-Hall, Inc., Englewood Cliffs NJ, 1974.
6. Dantzig, G., Orden A., and Wolfe, P., "Generalized Simplex Method for Minimizing a Linear Form Under Linear Inequality Constraints," *Pacific Journal Math.*, Vol. 5, pp. 183-195.